



Enhanced strengthening and hardening via self-stabilized dislocation network in additively manufactured metals

Zan Li ¹/_{**}, Yinan Cui ²/_{*}, Wentao Yan ³/_{*}, Di Zhang ¹, Yan Fang ⁴, Yujie Chen ⁴, Qian Yu ⁴, Ge Wang ¹, Heng Ouyang ¹, Chen Fan ³, Qiang Guo ¹, Ding-Bang Xiong ¹, Shenbao Jin ⁵, Gang Sha ⁵, Nasr Ghoniem ⁶, Ze Zhang ^{4,7}/_{*}, Y. Morris Wang ⁸/_{*}

The advent of additive manufacturing (AM) offers the possibility of creating high-performance metallic materials with unique microstructure. Ultrafine dislocation cell structure in AM metals is believed to play a critical role in strengthening and hardening. However, its behavior is typically considered to be associated with alloying elements. Here we report that dislocations in AM metallic materials are self-stabilized even without the alloying effect. The heating–cooling cycles that are inherent to laser power-bed-fusion processes can stabilize dislocation network in situ by forming Lomer locks and a complex dislocation network. This unique dislocation assembly blocks and accumulates dislocations for strengthening and steady strain hardening, thereby rendering better material strength but several folds improvements in uniform tensile elongation compared to those made by traditional methods. The principles of dislocation manipulation and self-assembly are applicable to metals/alloys obtained by conventional routes in turn, through a simple post-cyclic deformation processing that mimics the micromechanics of AM. This work demonstrates the capability of AM to locally tune dislocation structures and achieve high-performance metallic materials.

Keywords: Dislocation; Additive manufacturing; Metal; Strength; Ductility

Introduction

Since the proposition of dislocation slip in 1934 and its experimental verification by electron microscopy more than 20 years

later, materials scientists have been playing with dislocations to create high-performance metallic materials for decades. For example, conventional strengthening strategies, such as grain refinement, solid solution or precipitation strengthening, are associated with dislocation blockage through the introduction of extrinsic obstacles to dislocation motion [1,2]. Mainstream efforts have focused on tuning these external dislocation obstacles to modify dislocation behaviours, and hence engender speci-

¹ State Key Laboratory of Metal Matrix Composites, Shanghai Jiao Tong University, Shanghai 200240, China

² Department of Engineering Mechanics, Tsinghua University, Beijing 100084, China

³ Department of Mechanical Engineering, National University of Singapore, Singapore 117575, Singapore

⁴ Center of Electron Microscopy and State Key Laboratory of Silicon Materials, School of Materials Science and Engineering, Zhejiang University, Hangzhou 310027, China

⁵ Department of Material Science and Engineering, Nanjing University of Science and Technology, Nanjing 210094, China

⁶ Mechanical and Aerospace Engineering Department, University of California, Los Angeles, CA 90095, USA

⁷ Center for Hypergravity Experimental and Interdisciplinary Research, Zhejiang University, Hangzhou, 310027, China

⁸ Department of Materials Science and Engineering, University of California, Los Angeles, CA 90095, USA

^{*} Corresponding authors.

E-mail addresses: Li, Z. (njulizan@sjtu.edu.cn), Zhang, Z. (zezhang@zju.edu.cn), Wang, Y.M. (ymwang@ucla.edu).

[#] These authors contribute equally: Zan Li, Yinan Cui, Wentao Yan.

fic mechanical properties [3]. However, the role of dislocation manipulation is frequently considered as a result to be understood, instead of a tuneable degree of freedom that can be controlled by dislocation itself.

Additive manufacturing (AM), which is attractive for the production of three-dimensional parts with complex geometry, provides a new pathway for manipulating dislocation structures. In AM processing, powders are melted and solidified layer-wise, during which the built parts experience a specific thermal history [4-7]. First comes a rapid quenching from the melts, with a high thermal gradient, followed by cyclic heating-cooling during subsequent sample building. We recently showed that this repetitive and nonequilibrium build process produces tension-compression cycles in the solidified parts, leading to creation and selfassembly of high density of dislocations (Fig. 1(a)) [7]. Furthermore, many AM metallic materials that contain ultrafine dislocation cells tend to display extraordinary mechanical properties, which are not easily accessible by conventional processing methods (e.g., casting, cold- or hot-working, which typically lead to strength-ductility trade-off). Examples span typical AM materials including austenitic stainless steel (SS), high entropy alloys and Inconel alloys [8-13]. Yet detailed studies of the underlying mechanisms responsible for the superior properties remain scarce, with only limited insights into the importance of dislocation structure [8,9,14,15]. In addition, limited by the multielements nature of the mostly developed AM metallic materials, dislocation behaviours are largely determined by or coupled with alloying effects. Therefore, the nature of dislocation configurations and the associated deformation mechanisms are still open questions to AM community.

We here combined experimental investigations with simulations to revisit dislocation behaviours in AM materials, by using high-purity Cu (>99.9%) as a prototype. For the first time, the inherent ability of AM in creating metals with unique dislocation configuration is uncovered. We show that the dislocation cell structure is regulated in situ upon AM processing, leading to a self-strengthened, low-energy configuration in the as-built state. This new kind of dislocation network enables an unprecedented interplay between dislocation pinning, storage and nucleation, thereby resulting in superior mechanical properties as compared to traditional processing route. Our results unravel the ability of AM to locally tune the dislocation structure, and provide an alternate way of 'dislocation engineering' to prompt superior mechanical performances of metallic materials.

Materials and methods

Materials fabrication

We identified the processing window for porosity-free AM-Cu, using a laser powder-bed-fusion (L-PBF) printing system (S210, BLT). Spherical, high-purity Cu powders with a mean particle size of $\sim\!30~\mu m$ were prepared by a home-made electrode induction gas atomization (EIGA) system. The nominal powder composition, as measured by inductively coupled plasma mass spectrometry (ICP-MS, for conventional elements) and instrumental gas analysis (IGA, for O, N, H and S), was 0.0002 wt.% Al, 0.0001 wt.% Co, 0.0034 wt.% Fe, 0.0002 wt.% Mg, 0.0004 wt.% Zn and 0.0008 wt.% O. The balance is Cu

(>99.9%). The contents of other elements, such as C, H, S, were too low to be detected. We chose two processing windows to print AM-Cu with different dislocation densities, both of which were optimized for porosity-free samples (Fig. S1). The key printing parameters were provided in supplementary information (Table S1). A continuous scanning strategy with a rotation of 67 degrees for alternate layers was adopted in order to randomize crystal orientation and alleviate residual stress in the as-built samples, and the oxygen content in the chamber was controlled below 50 ppm. The density of the as-printed cuboidal Cu with sides of 20 mm was measured to be 99.5 \pm 0.2 %, using the Archimedes method. For comparative purposes, we obtained conventionally deformed Cu by firstly annealing high-purity wrought Cu at 900 °C for 1 h, followed by cold-rolling by 70% thickness reduction. The cold-rolled Cu (CR-Cu) were annealed at 150 °C with holding time of 5/10 mins, with the purpose to reach similar dislocation density and hardness to those of AM-Cu samples (see supplementary information, Table S2). To minimize oxidation, the annealing steps were conducted in a glove box with oxygen and water content less than 0.5 ppm.

Electron back scatter diffraction (EBSD) and transmission kikuchi diffraction (TKD)

EBSD was employed by a high-resolution EBSD system (Symmetry S2, Oxford), with an angular resolution below 0.05°. AZtecCrystal data processing software was used for EBSD data analysis. An accelerating voltage of 15 keV was used for EBSD data collection. Samples were prepared using standard metallographic techniques, where the sample surface was finally polished with the ion milling system (Model 1060, Fischione) to achieve a high validated hit rate (>99%). We employed TKD to analyse the microstructure and local misorientations of AM-Cu, with a Bruker OPTIMUS $^{\!\scriptscriptstyle{\text{TM}}}$ detector installed in a scanning electron microscopy (SEM) (MIRA3, Tescan). The microscope was operated at an acceleration voltage of 20 keV and a beam current of 6 nA. The orientation data during scanning were collected with a pattern resolution of 800×600 pixels (2 \times 2 binning). The exposure time was 20 ms and the scan step size was 8 nm. Data analysis was performed using OIM TSL software provided by EDAX. Grain boundaries (GBs) with misorientation angles between 2-10° and >10° were considered as low- and highangle GBs, respectively.

Transmission electron microscopy (TEM)

Bright-field TEM images of AM- and CR-Cu samples were performed by Thermo Fisher TALOS F200X at an accelerating voltage of 200 keV. The scanning TEM (STEM) images were recorded in a Cs-corrected JEOL JEM-ARM 200F fitted with an imaging aberration corrector (CEOS). High resolution STEM images, with a maximum point-to-point spatial resolution of 0.08 nm, were obtained with a convergence angle of 26 mrad and collection semi-angles from 50 to 180 mrad. TEM samples were prepared by the lift-out method using a focused-ion-beam (FIB) system. Nano-milling (Nanomill 1040, Fischione) operated at 800 V was employed to remove the surface amorphous layer produced by FIB milling.

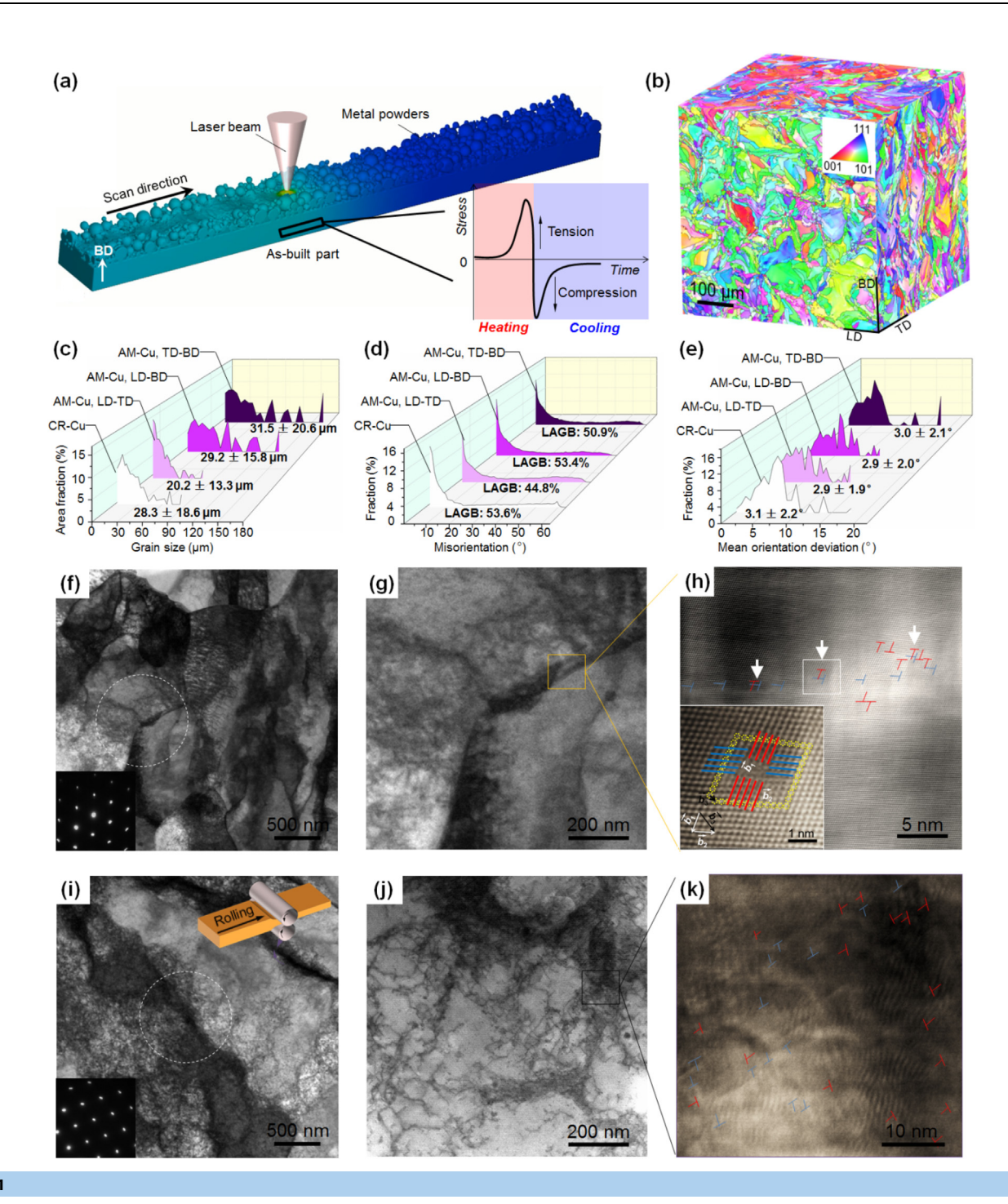


FIGURE 1

Additively manufactured and conventional deformation-produced high-purity Cu. (a) A schematic of the AM process including a sketch of the stress state experienced by solidified parts in front of the laser beam. One tension-compression cycle is applied once the laser beam scans over the surface due to large thermal gradient. Multiple tension-compression cycles upon sample building create dislocations with unique structure. Note that this simplified schematic does not consider the (re)melting/(re)solidification processes during AM. Sample building direction (BD) is indicated by the white arrow. (b) A 3D reconstruction of EBSD inverse-pole figure (IPF) maps of the as-built AM-Cu. High-angle grain boundaries (HAGBs) with misorientations larger than 10° are superimposed. (c)-(e) Statistical distribution of grain size (c), grain boundary misorientation (d) and mean orientation deviation (e) for AM-Cu with different planes and conventionally cold-rolled Cu (CR-Cu). Grain size in (c) is defined by HAGBs (misorientation angle larger than 10°). LD and TD are the lateral direction and transversal direction, respectively. LD-TD, LD-BD and TD-BD represent different normal planes as shown in (b). (f) A representative bright-field TEM image of dislocation cells in AM-Cu. Beam direction is along the [110] zone axis. Inset shows the SAED pattern of the circled region in (f), which contains a triple junction of cells. The aperture size for SAED is 1 µm. (g) An enlarged view of TEM image to show a typical dislocation cell in AM-Cu, revealing the sharp dislocation cell-wall morphology. (h) Aberration-corrected HAADF-STEM image of the cell-wall region shown in (g). Dislocations are arranged closely, with immobile dislocation locks (Lomer locks) frequently observed (indicated by white arrows). Inset shows the atomic structure of the selected region. The Burgers circuit analysis reveals the formation of a Lomer lock. (i) Bright-field TEM image of dislocation structure in CR-Cu, with the corresponding SAED pattern shown in the inset. Beam direction is along the [110] zone axis. (j) An enlarged view of TEM image to show a typical dislocation cell in CR-Cu. Dislocations are loosely packed and cell-wall is thick (tens of nanometers). (k) Aberration-corrected HAADF-STEM image of the cell-wall structure in (j), showing the sparse distribution of dislocations absent of mutual interactions. The raw STEM images are displayed in Fig. S4.

In situ TEM tensile tests

TEM samples were first polished with silicon carbide papers down to 80 μm and then punched into disks with a diameter of 3 mm. The disks were further thinned by electropolishing using 25% phosphoric acid, 25% ethanol and 50% distilled water to obtain thin regions for TEM observations. The polishing temperature was set to be $-20~^\circ C$. These polished disks were attached to stainless-steel substrates with narrow rectangular windows, enabling electron beam transmission. In situ uniaxial tensile tests were performed at ambient temperature in a FEI Tecnai G2 F20 TEM operating at 200 keV, using a Gatan 654 single-tilt straining holder.

Macroscopic tensile tests

Dog-bone specimens with 8 mm gauge length, 2 mm width, and 1 mm thickness were cut from the AM- and CR-Cu by electrodischarge machining (EDM). Tensile direction is vertical to the build direction for AM-Cu, and is aligned with rolling direction for CR-Cu. Surfaces and sides of the tensile samples were polished with 360–4000 European grit metallographic silicon carbide papers, followed by polishing in 3 μm and 1 μm diamond suspensions. The final thickness of the tensile specimens was $\sim\!0.9$ mm. Quasi-static uniaxial tensile tests were conducted in a universal testing machine (Instron 3344) at a constant strain rate of 5 \times 10 $^{-4}$ s $^{-1}$ at ambient temperature. At least five tensile tests were carried out to obtain statistical values. Tensile elongations were measured using a static axial clip-on extensometer (Model 2630-101, Instron) with 1 μm displacement resolution.

Multi-physics modelling of AM process

The evolution of individual powder particles during the AM process was simulated using a meso-scale thermal-fluid flow model. To ensure fidelity, the randomly packed powder bed was generated by simulating the powder spreading process with the experimentally measured powder size distribution, and most of the key physical parameters, such as laser heating, heat transfer, melting, molten pool flow and solidification, were incorporated. Furthermore, the temperature profiles from the thermal-fluid flow model were implemented into a finite element model to simulate the thermal stress distribution. The thermal-fluid flow simulations were performed on FLOW3D with extensive inhouse development, and the thermal-stress simulations were performed on ABAQUS with extensive in-house development as well. More details of our modelling framework can be found elsewhere [16].

Discrete dislocation dynamics (DDD) modelling

We developed a two-dimensional discrete dislocation dynamics method based on refs [17–21]. In this method, a given density of edge dislocations with an equal number of positive and negative Burgers vectors were randomly put in a square Cu cell with length 4 μm . The shear modulus and Poisson's ratio of Cu is 42 GPa and 0.34, respectively. Periodic boundary condition was employed to simulate the bulk material behavior. The starting dislocation structure evolves dynamically without external loading until a metastable configuration is obtained. Overdamped dynamics was assumed, such that dislocation velocity is proportional to the total force induced by the external loading and the

interactions with other dislocations. The viscous drag coefficient was taken to be 10^{-4} Pas. The edge dislocations with opposite Burgers vector annihilate each other when their distance is smaller than the annihilation distance $L_a=6b$. Here b is the magnitude of burgers vector. Dislocations can be generated from sources when the local resolved shear stress (τ) at the source location is higher than τ_c for a sufficiently long time t_c [18,21]. Dislocation sources with density of $\rho_{\rm nuc}$ were randomly introduced in slip planes to simulate the Frank-Read sources. Their strength τ_c follows a Gaussian distribution with mean value of 50 MPa and 10% standard deviation.

Results and discussion

Fabrication and microstructures

We built cuboidal L-PBF Cu parts with side-length of 20 mm. Due to low laser absorption in the near-infrared region (<10%), the production of near fully dense Cu is difficult for most L-PBF machines [22]. We identified optimized processing windows for AM-Cu (density: >99.2%), following the normalized equivalent energy density (E_0^*) approach (see supplementary information, Text S1) [23,24]. The E_0^* diagram helps to delineate the useful processing windows for AM-Cu with tuneable dislocation densities. We observed the combination of laser parameters that fall near the E_0 *~3 isopleth line is able to create AM-Cu with high dislocation density ($\sim 10^{15}~{\rm m}^{-2}$) and $E_0 \star \sim 9$ for low dislocation density ($\sim 4 \times 10^{14} \text{ m}^{-2}$), respectively (Fig. S1). They are named as AM-Cu-A and AM-Cu-B, respectively. The conventional coldrolled Cu samples, which possess similar dislocation density to those of AM-Cu-A or AM-Cu-B, are termed as CR-Cu-A and CR-Cu-B, respectively.

Fig. 1(b) shows EBSD images of AM-Cu, consisting of microstructures from three normal planes. It contains high fractions of low-angle grain boundaries (LAGBs, misorientation angle between 2-10°, ~40-50%) and grains are large, with an average grain size of ~30 μm. The grains exhibit a tortuous morphology for all planes, in stark contrast to the faceted nature in well annealed Cu [25]. The distribution of grain size is also non-uniform, where some large grains (size > 80 μm) can be observed. Large input energy in laser illumination with a high local thermal gradient renders strong fluid flow in the melt pool (Marangoni convection), which may perturb grain nucleation and growth kinetics during solidification, leading to the inhomogeneous grain distribution [6]. We found that the average grain size, LAGB fraction and mean orientation deviation (a grainbased misorientation difference between one specific point in a grain and the average orientation of the grain [26]) between AM- and CR-Cu are similar (Fig. 1(c-e)). However, further TEM examinations revealed that their dislocation configurations are remarkably different. Fig. 1(f) and (g) show that in the as-built AM-Cu dislocations are arranged into submicron dislocation cells, the majority of which are well-defined, akin to subgrains in severely plastically deformed (SPD) Cu [27,28]. The selected area electron diffraction (SAED) pattern encompassing parts of the three dislocation cells indicates that misorientations between them are below the resolution limit of SAED. This is in line with the presence of few LAGBs at the length scale of dislocation cells in high-resolution EBSD and TKD analyses (Figs. S2(c) and S3), but is counterintuitive because SPD metals that display sharp dislocation cell-walls usually contain detectable grain misorientations [28]. This confirms that these cell boundaries are not traditional dislocation cell-walls as observed in SPD metals. Normally, the sharp cell boundaries are counted as equilibrium boundaries, containing few excess dislocations to accommodate local misorientation across the cell boundary [28-30]. Dislocation density in cell-walls is too high for conventional weakbeam technique to work well. We therefore characterized the atomic structures of the cell-wall region using high-resolution STEM, Fig. 1(h), with the original STEM image displayed in Fig. S4(a). We found that cell-walls are generally pinned by some extrinsic dislocations that form Lomer locks, one representative atomic structure of which is displayed in the inset of Fig. 1(h). At least twenty STEM micrographs were carefully examined, and the formation of high-density of Lomer locks in dislocation cell-walls was proven to be a general feature. The inter-pinned dislocation configuration is neither attributed to O or N segregation at cell-walls, nor due to pinning of other alloying elements (e.g., Al, Co and Fe), as examined by atom probe tomography (APT, Fig. S5). While for CR-Cu with similar dislocation density, thick (tens of nm) and blurred dislocation cells prevail (Fig. 1(i) and (j)). Dislocations in cell-walls are loosely distributed to accommodate the local misorientations (Fig. 1(k)). The presence of large numbers of extrinsic dislocations in CR-Cu without discernible mutual trapping (shielding) is associated with a strong elastic strain field, leading to a high-energy state. Tilting of TEM samples indicates that the above differences in dislocation morphologies are physical and are not due to local projection effects.

Dislocation network stabilization mechanisms

The above results suggest the inherent nature of AM in tuning dislocation structures. Our multiphysics modelling demonstrates that a microscopic tension–compression cycle is generated as the laser beam is scanned over the surface, which produces dislocations in the solidified part (schematically shown in Fig. 1(a)) [7]. We estimated that at least 150 thermomechanical cycles are exerted upon sample building (Fig. S6). In this case, the back-and-forth gliding of dislocations can annihilate unstable dislocation dipoles and form sessile dislocation locks (Lomer locks), triggering the self-organization of dislocations into an inter-pinned configuration. The high-temperature environment upon sample building further accelerates this process. Thus, the relaxed, self-strengthened dislocation cells appear sharp in TEM observations.

We further employed DDD modelling to simulate the micromechanics associated with the layer-wise building process of AM. Dislocation multiplication and annihilation were both considered in our modelling framework. We show that the effect of cyclic heating–cooling, namely, tension–compression cycles, on dislocation network stabilization is manifested in the following three observations: (i) Initially, most dislocations are arranged into regular patterns (dislocation walls and cells) (Fig. 2(a)). The subsequent cyclic deformation processing (CP) conducted in the microplastic region triggers dislocation self-

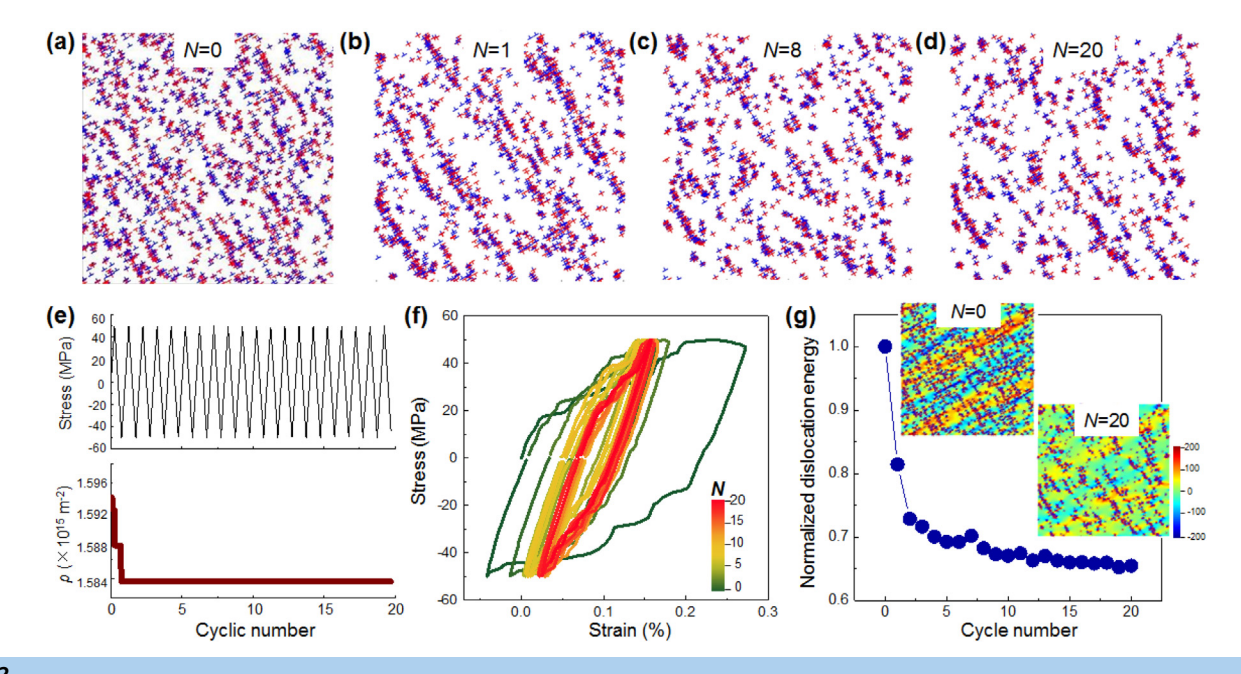


FIGURE 2

Dislocation network stabilization mechanisms. (a-d) Discrete dislocation dynamics (DDD) simulation results on dislocation patterns subjected to different numbers (N) of cyclic deformation processing (CP). Dislocation patterning in a two-dimensional configuration is carried out at (a) N = 0; (b) N = 1; (c) N = 8; (d) N = 20. Dislocation network stabilizes when N > 8. (e) The evolution of applied stress and dislocation density as a function of N. Note that dislocation density only decreases slightly from $1.5925 \times 10^{15} \text{ m}^{-2}$ at N = 0 to $1.58375 \times 10^{15} \text{ m}^{-2}$ at N = 20 (i.e., 0.5% reduction). (f) Stress–strain responses during CP at a constant stress magnitude of ± 50 MPa (in the micro-plastic region). The area enclosed by each stress–strain cycle firstly shrinks and gradually saturates with N, showing a 'cyclic-strengthening' feature. (g) Normalized dislocation energy (energy per dislocation normalized by its initial value at N = 0) as a function of N. The mutual, spontaneous interactions of dislocations shield them from the applied elastic field, resulting in a reduction in dislocation energy. Insets show simulated stress distributions (unit: MPa) of dislocation patterns before processing (N = 0) and after cyclic deformation with N = 20.

organization towards a stable configuration. Fig. 2(b-d) displays dislocation patterns at different cycle numbers (N), indicating that dislocation structure stabilizes after eight cycles (N = 8). Dislocation patterns with relatively large cycle number (N = 150) were also probed, showing marginal differences with those of N = 20. It is noticeable that, as displayed in Fig. 2(e), dislocation density changes marginally with cyclic deformation. This indicates that dislocations are not annihilated but are likely to be inter-pinned when cyclically loaded. (ii) With N increases, the stress-strain hysteresis loop gradually shrinks (Fig. 2(f)). The area enclosed by the stress-strain hysteresis loops reduces by 80% when N = 20. This observation lends direct support to our earlier claim that dislocation networks are strengthened upon AM processing. In consideration of the invariance in dislocation density, we thus believe that the strengthening of dislocation networks is solely associated with structural effects and are not due to dislocation accumulation upon processing. (iii) As shown in Fig. 2(g), the elastic energy per dislocation first displays a sharp decrement with N, followed by an almost constant value for N > 15; that is, dislocation structure is energetically stabilized with cyclic loading. This structure relaxation is also well embodied in stress distribution mapping as shown in the inset. The energy reduction is presumably originated from strong dislocation inter-pinning, which shields dislocation strain/stress fields to render a lower energy state. Altogether, our modelling results demonstrate that the microscopic cyclic loading that is inherent to AM stabilizes dislocation structure, both mechanically and energetically. This leads to the unique dislocation structure in AM Cu. We note here that our model above does not take into account the solidification/resolidification processes during L-PBF, which may lead to initial dendritic or columnar solidification morphology of dislocation cellular structures [13]. Such cellular structures can subsequently evolve under cycle loading. For CR-Cu, the cells form via deformation-induced nucleation and selfassembly, without solidification playing a role. This intrinsic difference between AM- and CR-processes is a topic worthy of further investigations.

Deformation behaviours of stabilized dislocation network

We performed in situ TEM tensile experiments to track microstructural evolutions of the self-stabilized dislocation network in AM-Cu, and compare it with the conventional dislocation cells in CR-Cu. At the very early stages of deformation, dislocations are found to pile-up at some of cell boundaries in AM-Cu (Fig. 3(a), white arrow), suggesting that stabilized cellwalls are strong dislocation obstacles. With increasing deformation, dislocation glide continues to be the dominant deformation mechanism; yet dislocations are terminated and stored at cell-walls without penetration into adjacent cells (Fig. 3(b)). Thus, dislocation activity is topologically confined to individual dislocation cells. The pinning of dislocations at cell-walls, which are strengthened by the immobile Lomer locks, is so strong that after de-pinning, dislocations move very rapidly across the cell interiors before being stored at the opposite cell boundary (see supplementary information, movie S1). Interestingly, the dislocation cells appear stable (i.e., little morphology change upon loading) and are likely to act as dislocation sources when the localized stress is high (at 10 s and 11 s in movie S1 and S2,

respectively). Thus, dislocation blockage, storage and nucleation are synchronously enabled in AM-Cu. The interplay of these mechanisms on one hand, promotes strengthening via enhanced resistance to dislocation penetration and trapping of dislocations at cell boundaries, and, on the other hand, alleviates serious stress concentrations to promote deformation homogenization. This might be responsible for the excellent strength-ductility synergy in many AM metallic materials containing pre-existing dislocation cells [15,31,32].

For conventionally cold-deformed Cu, however, dislocation network evolves actively upon straining (movie S3). The loosely-packed dislocation cell-walls are deficient in sessile Lomer locks, which are not sufficiently strong to resist dislocation motion. When subjected to external loads, dislocations can nucleate or escape at cell-walls, penetrating through neighbouring cells, and travelling long distances before being impeded at strong pinning points (Fig. 3(e)). This deformation feature leads to large dislocation mean free paths, which may suppress dislocation multiplication [33]. With straining, stress concentrations due to dislocation pile-ups can break up dislocation cellwalls, after which the dislocation activity in the un-constrained state becomes more extensive, as shown in Fig. 3(f) and movie S3. These dynamic responses of conventional dislocation structure differ significantly from those of AM-Cu; but are consistent with the reported intermittent dynamics of dislocation arrangements as probed by differential aperture x-ray microscopy [34]. Moreover, the lack of mutual trapping of dislocations leads to large stored energy, which creates high internal stresses and facilitates dislocation recovery. Thus, compared with AM-Cu, dislocation multiplication rate is low and annihilation rate is high in CR-Cu at similar deformation levels, both of which are unfavourable for dislocation storage. The unprecedented dislocation storage capacity in AM-Cu is revealed by the remarkable dislocation accumulations in the post-mortem TEM examinations (Fig. S7). Additionally, we employed electron channelling contrast imaging (ECCI) to examine microstructures of AM- and CR-Cu deformed at different strains (Fig. S8). We found that extensive slip bands were formed in CR-Cu even at a relatively small strain of ~1%; while for AM-Cu, no slip bands were visible up to a large tensile strain of 12%. These results are consistent with our in situ TEM observations, where dislocations in CR-Cu tend to glide longer distances without being stopped by dislocation cell walls. These different deformation behaviours between stabilized and conventional dislocation structures may also be well embodied through quantitative fractal analysis, which demonstrates dislocation ensembles on a larger scale [35–37].

The superiority of AM-Cu in stabilized deformation can be further supported by micropillar compression tests. Single-crystalline AM- and CR-Cu micropillars, with their [111] direction parallel to the uni-axial compression direction (as identified by EBSD, Fig. S9), are milled from as-built bulk samples. The compressive stress–strain response of AM-Cu micropillars demonstrates a higher hardening ability and smaller discrete strain bursts (which is caused by collective dislocation escape at free surfaces) as compared with that of CR-Cu (Fig. 3(g)). Also, it appears that there is no major shearing of AM-Cu micropillars after a compressive strain of 15%, but strain localization prevails for CR-Cu micropillars (Fig. 3(h) and (i)). These deformation

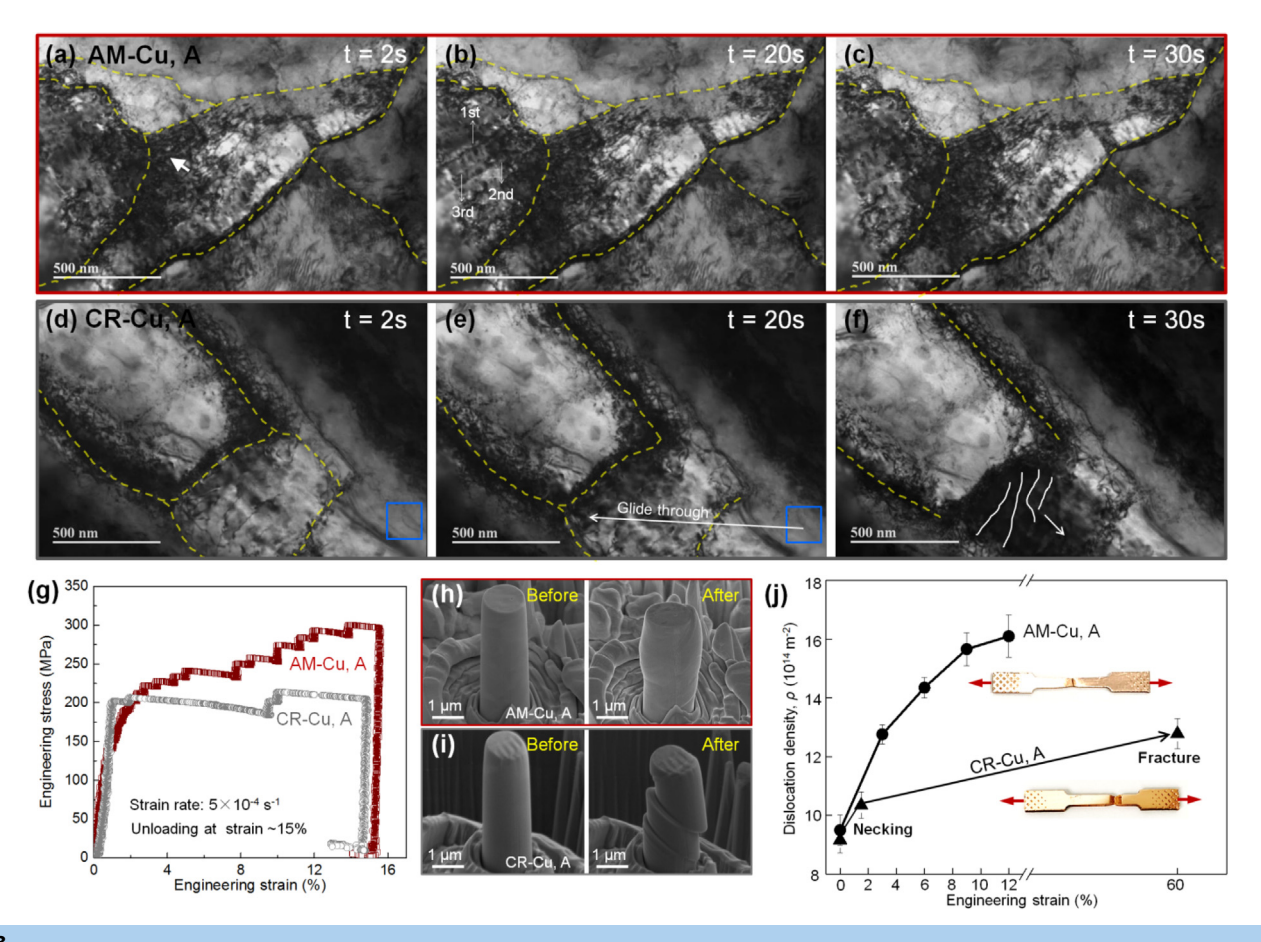


FIGURE 3

Deformation micro-mechanisms in AM- and CR-Cu. (a)-(c) Snapshots of in situ TEM tensile deformation of AM-Cu, showing the representative evolution of dislocation structures as a function of deformation. Dislocations are imaged under {111} type diffraction condition for clear identification. Dislocation cell-walls are sharp and are indicated by yellow dashed lines. Three dislocations (marked as 1st, 2nd, and 3rd) are travelled rapidly across the cell interiors and are impeded and stored at cell boundaries. Dislocation cells are stable throughout deformation. (d)-(f) Snapshots of in situ TEM tensile deformation of CR-Cu, revealing three typical deformation features. (1) The nucleated dislocation (in blue region in (d)) penetrates through dislocation cell-walls without obstruction and stops at strong obstacles. (2) Parts of the cell-wall in (e) are disappeared with straining. (3) Dislocation cell-wall breaks due to strong stress concentration, after which dislocations escape into cell interior (f). The dynamic process can be found in more detail in movie S3. (g) Compressive stress–strain responses of single-crystalline Cu micropillars. Single-crystalline micropillars with diameter of ~1.3 μ m and height of ~4 μ m are milled from polished AM- and CR-Cu surfaces using FIB, and are uni-axially compressed along [111] direction. The maximum engineering compressive strain is set to be 15%, and strain rate is $5 \times 10^{-4} \, \text{s}^{-1}$. AM-Cu shows higher hardening ability and much smoother plastic flow than CR-Cu. The lower yield strength of micropillars as compared with that in macro-tensile tests may be attributed to image force. (h), (i) SEM images of AM- and CR-Cu micropillars before and after compression, respectively. Note that no major shearing is observed for AM-Cu micropillars. (j) Dislocation density evolution for AM- and CR-Cu as a function of applied strain. AM-Cu demonstrates much higher dislocation accumulation rate than CR-Cu.

features are attributed to the fact that long-range gliding of dislocations is interfered by self-stabilized dislocation networks in AM-Cu via multiple cell-dislocation interactions, as demonstrated by the above in situ experiments, thereby leading to deformation homogenization. In addition, far more pronounced dislocation accumulation in AM-Cu is revealed by X-ray diffraction (XRD) analysis of the deformed bulk samples. Fig. 3(j) shows the evolution of dislocation density in AM- and CR-Cu as a function of applied strain (ε), as studied by XRD (the measurement details can be found in Supplementary Text 2 and in Fig. S10). We found that the flow stress in both samples follows the Taylor hardening equation, suggesting that dislocations act as the governing strengthening mechanism (see Supplementary Text 2 for more discussion). Prior to tension, both AM- and CR-Cu have high dislocation density ($\sim 0.9 \times 10^{15} \, \mathrm{m}^{-2}$). However, dislocation storage is much more extensive in AM-Cu than that in CR-Cu.

Mechanical properties

Fig. 4(a) shows the tensile properties of AM- and CR-Cu with identical pre-existing dislocation density. To emphasize the superiority of AM-Cu, we include two sets of comparisons that possess different yield strengths (~200 MPa and ~300 MPa). Tensile properties of AM-Cu are far super in both conditions, as indicated by the vastly higher ductility at similar yield strength compared to those of CR-Cu. In particular, AM-Cu-A (yield strength: 303 ± 12 MPa) reveals a factor of ten lager uniform elongation, reaching ~12–16%. The dramatic improvements in ductility correspond to higher strain hardening rates in AM-Cu (Fig. 4(a), inset), which presumably stem from the mechanically/energetically stable dislocation network. Fig. 4(b) demonstrates that our AM-Cu has superior improvements in strength-ductility combinations compared to those reported strategies based on dislocation strengthening [28,38–40]. Moreover, the

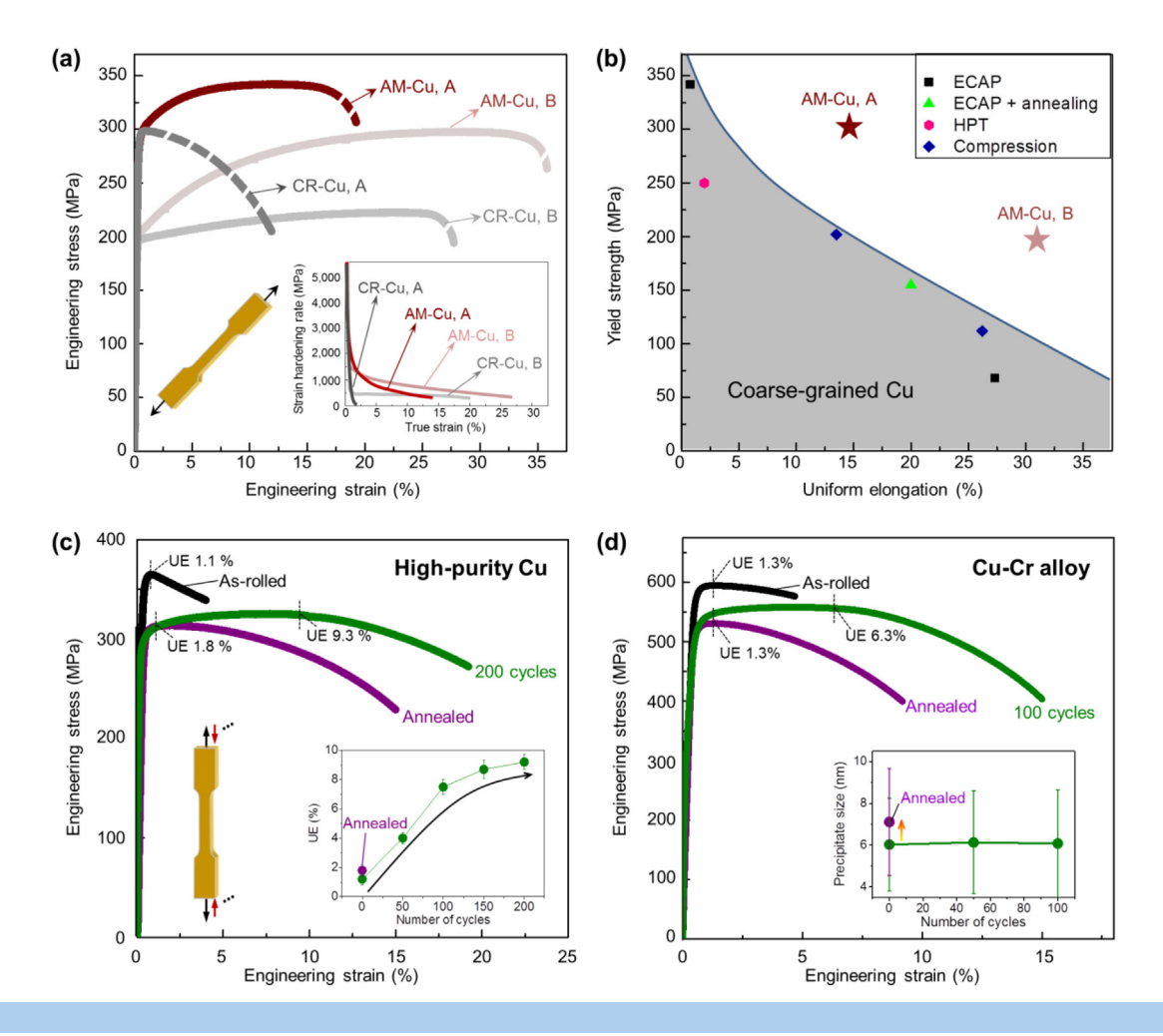


FIGURE 4

Mechanical responses. (a) Tensile engineering stress–strain curves of AM- and CR-Cu with different yield strengths (~200 MPa and ~300 MPa), respectively. Insets show strain hardening responses, where AM samples display significantly higher hardening capacity. (b) A summary of yield stress versus uniform elongation for dislocation-strengthened Cu fabricated by various strategies. These include equal channelling angular pressing (ECAP) [28], ECAP plus annealing treatment (ECAP+ annealing) [38], high-pressure torsion (HPT) [39] and compression densification (Compression) [40]. The outstanding combination of strength and ductility observed in AM-Cu exceeds those reported in these conventional fabrication strategies. Error bar of data point in our work is present in Table S1. (c) Mechanical response of high-strength CR-Cu subjected to traditional thermal treatments and the cyclic deformation processing (CP). Note that annealing method softens the material yet only slightly improves the uniform elongation. CP approach, although it experiences loss in yield strength due to dislocation recovery, achieves a much higher $\varepsilon_{\rm u}$ (9.3%) than typical annealing strategy. Inset shows the evolution of $\varepsilon_{\rm u}$ as a function of N. (d) Tensile stress–strain responses of high-strength Cu-Cr alloy with different processing strategies. The result shows that CP approach is generally applicable for this representative alloy for enhanced strengthening. Inset displays precipitate size evolution with CP and conventional heat treatment. The statistical calculations were conducted by APT (see supplementary information for more details).

tensile properties of AM-Cu reported here are mainly aimed to demonstrate the proof-of-principle, and further property improvements are possible if dislocation structures in AM-Cu are optimized further. In spite of this, the tensile properties of AM-Cu have already surpassed or rivalled many wrought Cu alloys (Cu-Zn and Cu-Ni alloy [41], for example).

The intrinsic dislocation manipulation strategy in AM is extendable to the conventional dislocation-strengthened metallic materials. We applied an alternating stress using a universal fatigue machine to induce microscale tension–compression cycles on CR-Cu, mimicking the micromechanics of AM process except for the temperature effects (see supplementary information for more details, Text S3). The back-and-forth movement of dislocations enables dislocation re-arrangements and interpinning, forming a low-energy, sharp-contrast dislocation network (Fig. S11). The resultant tensile properties show that the

uniform elongation of CR-Cu is rejuvenated, reaching 9% after 200 tension-compression cycles, much higher than those for as-deformed state and heat-treatment sample (less than 2%, Fig. 4(c)). Furthermore, this strategy is also applicable to alloys. As an example, the precipitate-hardened Cu-Cr alloy improves its strength by deformation such as SPD or CR [42,43], but this greatly reduces its tensile uniform elongation (Fig. 4(d), black curve). Yet after cyclic deformation, it has nearly four folds improvement in uniform elongation (from 1.3% to 6.3%) without much sacrifice in tensile strength. It also demonstrates much superior properties over its heat-treated counterparts (Fig. 4(d), purple curve). The major advantage of this dislocation manipulation strategy relies on the fact that it is performed at ambient conditions, which separates dislocation processing without compromising other microstructural features (e.g., precipitate coarsening, inset of Fig. 4(d)). The cyclic deformation (in

comparison with the monotonic tension/compression) has at least two advantages. First, the back-and-forth movement of dislocations during the tension–compression cycles is preferable for the formation of sessile dislocation locks and other low-energy dislocation assemblies, as demonstrated by experimental observations in this work and in previous computational simulations [44–46]. Second, multiple tension–compression cycles allow for a large amount of strains without fracture, offering more space for dislocation self-assembly.

Conclusions

We have shown here that dislocation structures in AM metallic materials are self-stabilized via the nonequilibrium, layer-wise fabrication technique. Our work gained new insights on the unique configuration and beneficial effects of dislocation network in AM metals, by using the simplest Cu as a prototype to circumvent alloying effects. We found that dislocation cells are intrinsically present in the as-built Cu, whose structure is in situ strengthened by forming Lomer locks and dislocation re-arrangement upon building, making them both mechanically and energetically stable. This effect leads to a high work hardening capacity and high ductility in AM-Cu. Our findings shed lights on the excellent mechanical properties discovered in many other AM metallic materials. The thermomechanical cycles during AM, and consequently, localized dislocation structures can be tailored by a variety of processing parameters, making the present strategy desirable for practical applications. Therefore, dislocation manipulation by AM opens up a research area of both fundamental and applied importance. Furthermore, the current findings not only show how the strength-ductility trade-off can be successfully overcome for AM metals, but also elucidate new strengthening and hardening mechanisms based on selfstabilized dislocation network. Thus, mechanical property optimization by dislocation manipulation is different from other generally employed approaches such as heterogeneous structure design and interface engineering [47-52], and can provide an alternative direction for tuning microstructures to prompt superior mechanical performances of metallic materials.

Data and materials availability

All data needed to evaluate the conclusions in the paper are present in the paper and/or the Supplementary Information. Additional data related to this paper may be requested from the authors.

CRediT authorship contribution statement

Zan Li: Conceptualization, Supervision, Investigation, Writing-original draft. Yinan Cui: Methodology, Software, Writing-original draft. Wentao Yan: Methodology, Software, Data curation. Di Zhang: Supervision, Project administration. Yan Fang: Investigation. Yujie Chen: Investigation, Resources. Qian Yu: Investigation, Writing - original draft. Ge Wang: Investigation, Resources. Heng Ouyang: Investigation. Chen Fan: Methodology, Software. Qiang Guo: Investigation. Ding-Bang Xiong: Investigation. Shenbao Jin: Investigation, Visualization. Gang Sha: Investigation, Data curation. Nasr Ghoniem: Writing - review & editing. Ze Zhang: Vali-

dation, Writing - review & editing. **Y. Morris Wang:** Conceptualization, Writing - original draft.

Declaration of Competing Interest

The authors declare that they have no known competing financial interests or personal relationships that could have appeared to influence the work reported in this paper.

Acknowledgements

We thank Y. Han and X. Fu at Shanghai Jiao Tong University for their help with EBSD experiments and results discussion. We are grateful to Y. Yang at Bruker (Shanghai) Scientific Technology Co., Ltd for her help with TKD sample characterizations and results analyses. This research is supported by National Natural Science Foundation of China (Grant Nos. 51801120, 51971131 and 51821001).

Appendix A. Supplementary data

Supplementary data to this article can be found online at https://doi.org/10.1016/j.mattod.2021.06.002.

References

- A. Argon, Strengthening Mechanisms in Crystal Plasticity, Oxford University Press, Oxford, 2012.
- [2] M.A. Meyers, K.K. Chawla, Mechanical Behavior of Materials, Cambridge University Press, Cambridge, 2008.
- [3] J.P. Hirth, L. Kubin, Dislocation in Solids, Elsevier, Amsterdam, 2009.
- [4] C.Y. Yap et al., Appl. Phy. Rev. 2 (2015) 041101.
- [5] P. Kürnsteiner et al., Nature 582 (2020) 515-519.
- [6] L. Aucott et al., Nat. Commun. 9 (2018) 5414.
- [7] G. Wang et al., Mater. Res. Lett. 8 (2020) 283–290.
- [8] Y.M. Wang et al., Nat. Mater. 17 (2018) 63–71.
- [9] L.F. Liu et al., Mater. Today. 21 (2018) 354–361.
- [10] Z.G. Zhu et al., Scr. Mater. 154 (2018) 20–24.[11] H. Wang et al., Acta Mater. 196 (2020) 609–625.
- [12] T.G. Gallmever et al., Addit, Manuf, 31 (2020) 100977.
- [13] K.M. Bertsch et al., Acta Mater. 199 (2020) 19–33.
- [14] M. Shamsujjoha et al., Metall. Mater. Trans. A 49A (2018) 3011–3027.
- [15] Z. Li, B. He, Q. Guo, Scr. Mater. 177 (2020) 17–21.
- [16] W. Yan et al., Comput. Mech. 61 (2018) 521-541.
- [17] R. Amodeo, N. Ghoniem, Phy. Rev. B 41 (1990) 6968.
- [18] S. Akhondzadeh et al., Model. Simul. Mater. Sc. 26 (2018) 065011.
- [19] E. Van der Giessen, A. Needleman, Model. Simul. Mater. Sc. 3 (1995) 689.
- [20] M. Ovaska, L. Laurson, M.J. Alava, Sci. Rep. 5 (2015) 1–8.
- [21] H. Song, D. Dimiduk, S. Papanikolaou, Phy. Rev. Lett. 122 (2019) 178001.
- [22] P.A. Lykov, E.V. Safonov, A.M. Akhmedianov, Mater. Sci. Forum 843 (2016) 284–288.
- [23] J.C. Ion, H.R. Shercliff, M.F. Ashby, Acta Metall. 40 (1992) 1539–1551.
- [24] M. Thomas, G.J. Baxter, I. Todd, Acta Mater. 108 (2016) 26–35.
- [25] T. Konkova et al., Acta Mater. 58 (2010) 5262–5273.
- [26] M.N. Gussev, K.J. Leonard, J. Nucl. Mater. 517 (2019) 45–56.
- [27] J.Y. Huang et al., Acta Mater. 49 (2001) 1497–1505.
- [28] F. Dalla Torre et al., Acta Mater. 52 (2004) 4819–4832.
- [29] R.Z. Valiev, V.Y. Gertsman, O.A. Kaibyshev, Phys. Status. Solidi. A 97 (1986) 11– 56.
- [30] R. Valiev, Nat. Mater. 3 (2004) 511-516.
- [31] M.A. Melia et al., Addit. Manuf. 29 (2019) 100833.
- [32] M.E. Aydinoz et al., Mater. Sci. Eng. A 669 (2016) 246-258.
- [33] B. Devincre, T. Hoc, L. Kubin, Science 320 (2008) 1745–1748.
- [34] B. Jakobsen et al., Science 312 (2006) 889-892.
- [35] K. Siu, A. Ngan, Philos. Mag. 91 (2011) 4367-4387.
- [36] K. Siu et al., Int. J. Plast. 27 (2011) 788-800.
- [37] K, Siu, et al., Materialia 5 (2019) 100214.
- [38] Y.M. Wang et al., Nature 419 (2002) 912–915.
- [39] K. Edalati, T. Fujioka, Z. Horita, Mater. Sci. Eng. A 497 (2008) 168–173.[40] Y.S. Li et al., Scr. Mater. 59 (2008) 475–478.
- [41] J.P. Davis, Copper and Copper Alloys (ASM International, 2001).

- [42] C.Z. Xu et al., Mater. Sci. Eng. A 459 (2007) 303-308.
- [43] A. Meng et al., Vacuum 167 (2019) 329–335.
- [44] T. El-Achkar, D. Weygand, Modell. Simul. Mater. Sci. Eng. 27 (2019) 055004.
- [45] S. Brinckmann et al., Int. J. Fatigue 33 (2011) 1369–1375.
- [46] M. Sauzay, L.P. Kubin, Prog. Mater. Sci. 56 (2011) 725–784.
- [47] E. Ma, X.L. Wu, Nat. Commun. 10 (2019) 5623.

- [48] Y.J. Wei et al., Nat. Commun. 5 (2014) 3580.
- [49] X.Y. Li et al., Nat. Rev. Mater. 5 (2020) 706–723.
- [50] Y.M. Wang et al., Proc. Natl. Acad. Sci. USA 104 (2007) 11155–11160.
- [51] Z. Li et al., Nano Lett. 18 (2018) 6255–6264.
- [52] X.Y. Li, K. Lu, Nat. Mater. 16 (2017) 700-701.